iScience

CellPress
OPEN ACCESS

Article

Strategies for chemical vapor deposition of two-dimensional organic-inorganic halide perovskites

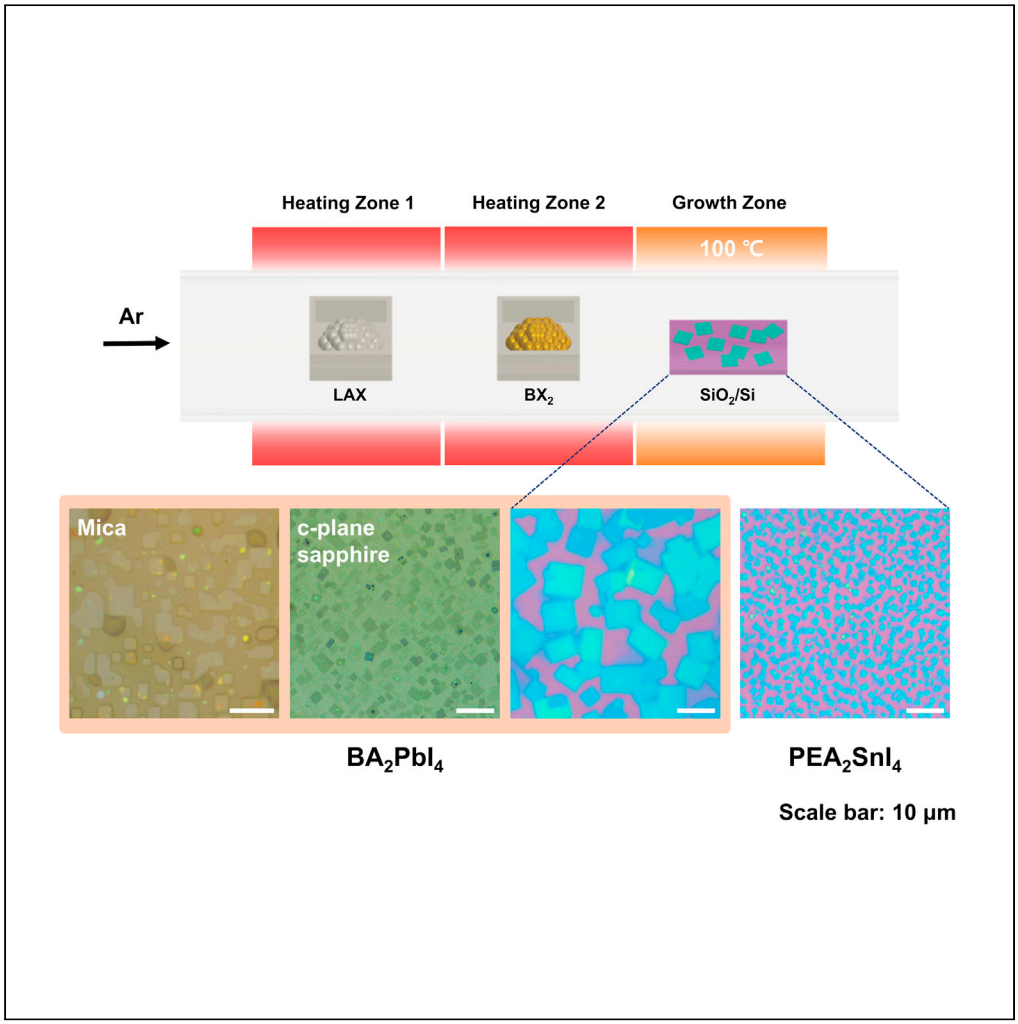

Ayoung Ham, Tae Soo Kim, Minsoo Kang, Himchan Cho, Kibum Kang

kibumkang@kaist.ac.kr (K.K.)
himchan@kaist.ac.kr (H.C.)

Highlights

CVD strategies for 2D OIHP growth are introduced

Temperature dependences of CVD-grown BA_2PbI_4 are discussed

Epitaxial growth of BA_2PbI_4 is observed on mica and c-plane sapphire

CVD-grown 2D tin-OIHP (PEA_2SnI_4) is demonstrated

Ham et al., iScience 24, 103486
December 17, 2021
https://doi.org/10.1016/j.isci.2021.103486

iScience

CellPress
OPEN ACCESS

Article

Strategies for chemical vapor deposition of two-dimensional organic-inorganic halide perovskites

Ayoung Ham,[1] Tae Soo Kim,[1] Minsoo Kang,[1] Himchan Cho,[1,*] and Kibum Kang[1,2,*]

SUMMARY

Two-dimensional (2D) organic-inorganic halide perovskites (OIHPs) with an alternating stacked structure of an organic layer and an inorganic layer draw significant attention for photovoltaics, multiple quantum-well, and passivation of three-dimensional perovskites. Although the low-cost and simple spin-coating process of these materials offers a vast platform to study fundamental properties and help them achieve rapid progress in electronics and optoelectronics, chemical vapor deposition (CVD) growth is also necessary for large-area, epitaxial, selective, and conformal growth. Here, one-step CVD strategies for 2D OIHP growth are proposed, and the growth trends depending on the precursor and substrate conditions are discussed. We report a CVD-grown nontoxic, lead-free 2D tin-OIHP flake to show the system offering a universal route to synthesize perovskite crystals based on arbitrary organic and inorganic components.

INTRODUCTION

Three-dimensional (3D) organic-inorganic halide perovskites (OIHPs) have been actively studied due to their remarkable performance in photovoltaics and electronics (Cho et al., 2015; Tan et al., 2016; Yuan et al., 2016). Behind the rapid advances, there are intriguing semiconducting properties, such as high carrier mobility, long carrier diffusion length, and large absorption coefficient. Recently, diverse applications, such as thermoelectricity and ferroelectricity with ultra-low thermal conductivity and large polarization, have been steadily reported, and OIHPs have been highlighted as potential semiconducting materials (Haque et al., 2020; Ye et al., 2016).

However, 3D OIHPs exhibit poor stability, which limits large-scale applications. Moreover, they are vulnerable to water, thermal stress, light, and electric fields (Cho et al., 2018; Conings et al., 2015; Eames et al., 2015; Huang et al., 2017; Lai et al., 2018). H_2O irreversibly decomposes perovskites into CH_3NH_3X, $CH(NH_2)_2X$ (X = halide) and PbX_2. In addition, electric-field- and photo-induced halide ion migration easily occurs, causing charge hysteresis, phase separation, and photo-instability. Recently, considerable research has been conducted to enhance the stability of perovskite devices (Cho et al., 2018; Kaltenbrunner et al., 2015; McMeekin et al., 2016). One of the proposed strategies to achieve this goal is the use of a 2D perovskite. In 2D perovskites, hydrophobic organic cations passivate the inorganic slab, which makes the perovskites air and water resistant. For this reason, they have been used in photovoltaics and electronics fields independently (Matsushima et al., 2016) or as a 2D/3D mixed-dimensional structure (Grancini et al., 2017; Lin et al., 2018) to overcome the stability issue. Layered perovskites (which are formed by dividing an inorganic bulk into slabs by an organic spacer), including 2D perovskites, are generally referred to as Ruddlesden-Popper (RP) phase perovskites.

2D lead perovskites have demonstrated outstanding performance in photovoltaics and electronics fields. For stabilization of perovskites, cation engineering and 2D/3D heterostructure fabrication have been implemented (Chen et al., 2017a; Grancini et al., 2017). Other stabilization methods include increasing the number of layers (Lee et al., 2019) and using 2D perovskites as doping agents (Lin et al., 2018). However, the toxicity of lead hinders commercialization of lead halide perovskites; as alternatives, environmentally benign lead-free perovskites have been studied (Cao et al., 2017; Cheng et al., 2017; Gao et al., 2019b). Among many candidates, tin perovskites have been spotlighted for the following reasons: first, homovalent substitution from Pb^{2+} to Sn^{2+} maintains 3D electronic dimensionality. Also, tin has a similar ionic radius

[1]Department of Materials Science and Engineering, Korea Advanced Institute of Science and Technology (KAIST), 291 Daehak-ro, Yuseong-gu, Daejeon 34141, Republic of Korea

[2]Lead contact

*Correspondence: kibumkang@kaist.ac.kr (K.K.), himchan@kaist.ac.kr (H.C.)

https://doi.org/10.1016/j.isci.2021.103486

(118 pm) compared with that of lead (119 pm), leading to highly symmetric perovskite structure with a reasonable tolerance factor (Ning and Gao, 2019). However, electronics applications of tin perovskites have shown limited success due to the poor film coverage and nonuniformity of tin perovskite films, resulting from uncontrollable crystallization during spin-coating (Hao et al., 2014). Furthermore, Sn^{2+} can be easily oxidized to Sn^{4+} under ambient conditions, requiring inert and dry growth conditions, which limits morphological control investigations. To improve the film quality, solvent engineering (Hao et al., 2015) and vapor-assisted solution process (Yokoyama et al., 2016) have been attempted. Vapor deposition of perovskites is an effective way to control the crystallization of perovskites and achieve uniform film morphology. Considering the great progress on vapor deposition techniques of lead perovskites, such as high-vacuum thermal co-evaporation (Liu et al., 2013) and chemical vapor deposition (CVD) (Luo et al., 2017), vapor deposition of tin perovskites may open a new route to control their film morphology for electronics and optoelectronics applications.

In particular, the CVD growth of 2D lead perovskite has been used to improve the quality of flakes and tailor their dimensionality from 0D to 3D. For example, Chen et al. synthesized BA_2PbI_4 epitaxially on mica (Chen et al., 2017b) and Ghoshal et al. succeeded in the growth of BA_2PbI_4 nanowires (Ghoshal et al., 2019). CVD of 2D OIHP is also needed for large-area, selective and conformal growth. However, understanding of growth behaviors for such advanced growth is still lacking.

This paper reports the gas-phase growth of 2D OIHPs, focusing on the growth behaviors and mechanisms. As the zone temperatures of organic precursors, halide precursors, and substrates can be precisely and independently controlled using a three-heating-zone CVD system, we present the growth trends (i.e., temperature dependence and substrate dependence) of 2D OIHPs with BA_2PbI_4 as a model system. In particular, the CVD growth of PEA_2SnI_4, which is a representative 2D lead-free perovskite material, is successfully demonstrated. We believe that our study can provide a general route and important strategies for the growth of arbitrary 2D OIHPs.

The article is composed of the following four sections. We will first present the structure and property information in "Background information on RP perovskites." "Three-heating-zone vapor deposition system and BA_2PbI_4 growth" outlines the schematics and results of BA_2PbI_4 growth, as well as temperature and substrate dependence. The trends of precursor growth and the final lead-free tin-perovskite growth are demonstrated in "Generality of the system: PbI_2 and PEA_2SnI_4 growth." In "conclusion," we summarize our experimental results and indicate that CVD strategies can provide a universal route to grow 2D OIHPs, which can be used in future electronics and optoelectronics.

Background information on RP perovskites

Crystal structure

The general chemical formula of 3D OIHPs is ABX_3, where A is a small monovalent cation such as Cs^+, $CH_3NH_3^+$, or $HC(NH_2)_2^+$; B is a divalent metal cation such as Pb^{2+} or Sn^{2+}; and X is a halide, such as Cl^-, Br^-, or I^- (Figure 1A). The B cation coordinates with six X anions to form an octahedra, and the A cation is placed in a cavity formed by the eight-corner-shared $[BX_6]^{4-}$ octahedra. To maintain the structural stability of the 3D lattice, the Goldschmidt tolerance factor calculated from the radii of the A, B, and X ions must be greater than 0.71, and the size of the A cations must be limited to <2.6 Å. When the cations have a large size, they act as a spacer of the inorganic slab to form a low-dimensional perovskite, RP phase $LA_2A_{n-1}B_nX_{3n+1}$ (LA: long-chain aliphatic or aromatic alkylammonium cation, n: number of $[BX_6]^{4-}$ sheets in a single inorganic slab). A complete 2D perovskite (n = 1) without the A cation exhibits a LA_2BX_4 structure, and a perovskite with $n \geq 2$ is called a mixed-dimensional 2D/3D (quasi-2D) perovskite. As shown in Figure 1C, the organic layer and multi-sheet inorganic layer are alternately repeated, and the layered structure is maintained by the van der Waals (vdW) force between the organic groups.

Several criteria are required to form an RP perovskite. First, each organic molecule needs to contain more than one terminal cation to form a hydrogen bond with the halide anions of the inorganic layer. Most of the well-known RP perovskites are denoted as $(RNH_3)_2BX_4$, terminating with a protonated primary amine. Second, it is a necessity for the organic molecules to be properly fitted into the terminal halide framework of the inorganic layer. When the cross-sectional area of a molecule is small, the structure is accommodated by tilting or interdigitating the organic molecules, and when the cross-sectional area is large, it cannot overcome the steric hindrance caused by the neighboring molecules, which results in a different type of

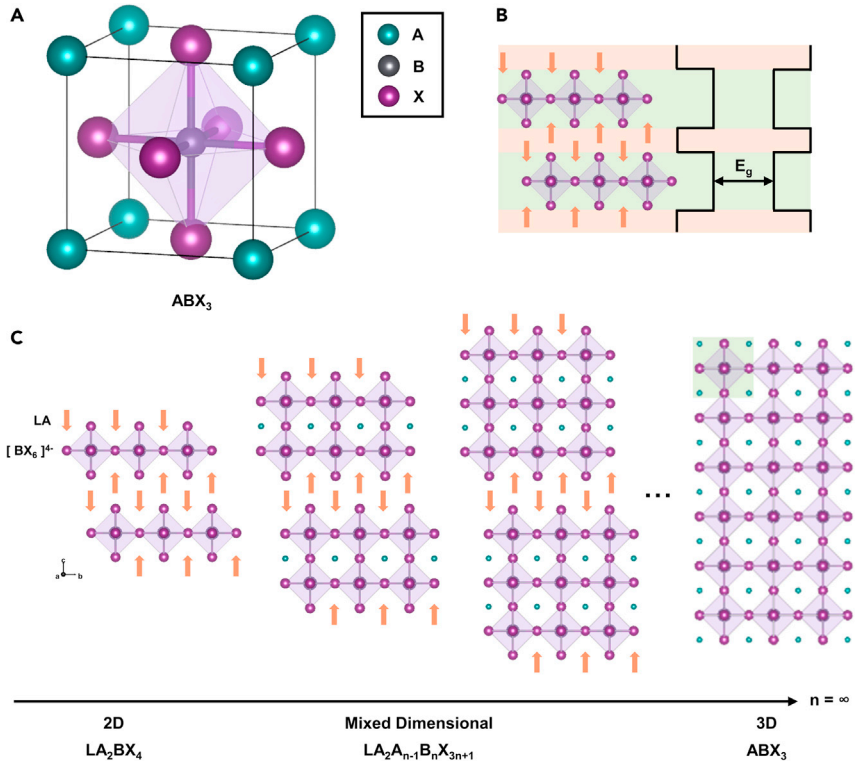

Figure 1. Crystal structures of RP perovskite

(A) Unit cell of an ideal 3D cubic perovskite ABX_3. A is an organic cation, B is a metal cation, and X is a halide.

(B) Band alignment of 2D perovskite results in natural multiple quantum well.

(C) Schematic illustration of RP phase perovskite from n = 1 (2D perovskite, LA_2BX_4) to n = ∞ (3D perovskite, ABX_3) viewed along the projection to the a axis. LA is a long-chain aliphatic or aromatic alkylammonium cation. Mixed-dimensional perovskites have $LA_2A_{n-1}B_nX_{3n+1}$ structure.

structures. However, the length of the organic molecule along the z axis can vary because the distance between the inorganic sheets can be adjusted according to the length.

Intrinsic and optoelectrical properties of RP perovskites: double-edged sword

RP perovskites exhibit several interesting properties, such as structural flexibility, multiple quantum-well structures, and large exciton binding energy, because of the LA organic layer acting as a spacer. Considering they are layered materials bound by the vdW force generated between the LA cations, they exhibit all basic characteristics of well-known vdW 2D materials, such as graphene and transition metal dichalcogenide (TMDC) (Song et al., 2020). Given the relatively weak vdW interaction between the substrate and film, broad film selection and easier film transfer are possible, and crystallization of the nuclei occurs well even on an amorphous substrate. Moreover, its exfoliation is facile and an ultrathin monolayer synthesis is available, which makes an RP perovskite a promising material for studying monolayer physics and heterostructures through vdW stacking without any lattice mismatch with other 2D materials (Dou et al., 2015; Pan et al., 2021).

Structural flexibility with a diverse combination of LA, A, and B cations and halide anions is another strength of an RP perovskite. Electrical and optical properties, such as bandgap and absorption, depend on the type of LA functional group used, and the way LA cation layers interact with each other (e.g., hydrogen bonding and π-π conjugations) determines the overall stability of the structure. By introducing a small A cation (i.e., increasing the number of layers n), the valence-band maximum and conduction-band minimum energy level can be engineered. Moreover, by controlling the doping level, the charge-carrier and defect density can be further adjusted, thereby broadening the range of band alignment management (Ball and Petrozza, 2016). Thus, an RP perovskite expands the field of semiconducting subgroups more diversely through composition tuning.

Furthermore, an RP perovskite exhibits a natural multiple quantum-well structure because $[BX_6]^{4-}$ layers are sandwiched between two LA cation layers. In this case, an inorganic slab with a small bandgap functions as a potential well, whereas an organic spacer with a large bandgap acts as a potential barrier (Figure 1B) (Gao, et al., 2019a). Semiconductor quantum-well structures and superlattices are key building units in optoelectronics, but for conventional materials, such as group III–V semiconductors, it is difficult to grow wells and barriers epitaxially and to control the thickness of each layer precisely (Yang et al., 2001). In contrast, the structure of RP perovskite can be easily formed by direct spin-coating, where n can be determined just by simply matching the stoichiometry of the precursor, so the desired thickness can be uniformly obtained for each slab. Furthermore, the wide range of LA options gives the freedom to control the band type and LUMO and HOMO energy levels of the barrier (Gao et al., 2019a).

As compared with 3D perovskites, the quantum-well structure of RP perovskites imparts a large exciton binding energy in contrast. Once excitons are generated, they confine to the inorganic layer under the quantum confinement effect resulting from the dielectric mismatch between the organic and inorganic layers. As this effect decreases with an increase in the thickness of the inorganic well, the exciton binding energy decreases with an increasing value of n (Brehier et al., 2006; Zhang et al., 2018). A larger exciton binding energy in the smaller n phase can also be explained by the local electric field generated by the LA layer (positively charged) and the $[BX_6]^{4-}$ layer (negatively charged), which is larger for a smaller value of n, increasing the suppression of the separation of electron-hole pairs. Consequently, when n = 1, exciton binding energy has a size of a few hundreds of milli-electron volts, an order of magnitude larger than that of bulk perovskite, but when n > 4, the size decreases to tens of milli-electron volts. If n > 10, the charge-carriers behave as free carriers, not excitons. Some RP perovskites have exciton binding energy values comparable with those of monolayer TMDC (Chen et al., 2017b; Hill et al., 2015), and the large exciton binding energy makes them stable excitons at room temperature (RT). Hence, an RP perovskite is a promising material for light-emitting applications and provides a platform to study excitonic processes such as polaritons and Bose-Einstein condensate over less stringent temperature ranges.

Meanwhile, LA organic layers are also a factor influencing efficiency deterioration in photovoltaics and electronics (Gélvez-Rueda et al., 2017; Tsai et al., 2018). 2D perovskites have a large bandgap and low carrier mobility due to their high organic content, which results in performance degradation. For solar cells, there is an optimum bandgap (1.4 eV) of the light absorber layer where the absorption is maximized, but with a pure 2D phase, the absorption is narrower because of the large bandgap. The charge-carrier extraction efficiency is also lowered by the strong exciton binding energy and the LA layer that blocks the charge transport, leading to a relatively small fill factor and photocurrent.

To address the aforementioned problems, a mixed-dimensional hybrid perovskite, having the advantages of both 2D and 3D perovskites, has been proposed (Jang et al., 2021). In high n value of mixed-dimensional perovskite $LA_2A_{n-1}B_nX_{3n+1}$, the 2D portion increases stability, and the large 3D portion overcomes the efficiency degradation caused by the organic layer (Cao et al., 2015; Fakharuddin et al., 2019; Yang et al., 2018). The first mixed-dimensional perovskite was proposed by Smith et al. by synthesizing $PEA_2MA_2Pb_3I_{10}$ (n = 3) to fabricate a solar cell. The $PEA_2MA_2Pb_3I_{10}$ crystal synthesized by one-step spin-coating with a precursor, which is a mixture of phenethylammonium iodide (PEAI) and methylammonium iodide (MAI) in a solvent, had a bandgap size between those of PEA_2PbI_4 and $MAPbI_3$ and maintained structural robustness for 46 days under air exposure with a relative humidity (RH) level of 52% (Smith et al., 2014). Since then, many attempts have been made to obtain an optimum structure that can secure stability and minimize performance degradation. For example, Chen et al. synthesized $(iso\text{-}BA)_2MA_3Pb_4I_{13}$ by adopting a short-branched cation iso-butylammonium ($iso\text{-}BA^+$) as a spacer to increase optical absorption, which maintained absorption for 840 h at 20°C and 60 RH without encapsulation (Chen et al., 2017a). Wang et al. introduced an n-butylammonium (BA^+) cation to $FA_{0.83}Cs_{0.17}Pb(I_yBr_{1-y})_3$, which is a mixed-cation lead mixed-halide perovskite exhibiting controlled stoichiometry of A cation or X anion. The resulting mixed-phase $BA_x(FA_{0.83}Cs_{0.17})_{1-x}Pb(I_{0.6}Br_{0.4})_3$ guaranteed both stability and efficiency (Wang et al., 2017).

RESULTS AND DISCUSSION

Three-heating-zone vapor deposition system and BA_2PbI_4 growth

Growth schematics and results

Figure 2 shows the CVD setup for RP perovskite growth and the morphology of as-grown BA_2PbI_4 flakes along with their characterization. Figure 2A schematically illustrates the CVD setup for one-step BA_2PbI_4

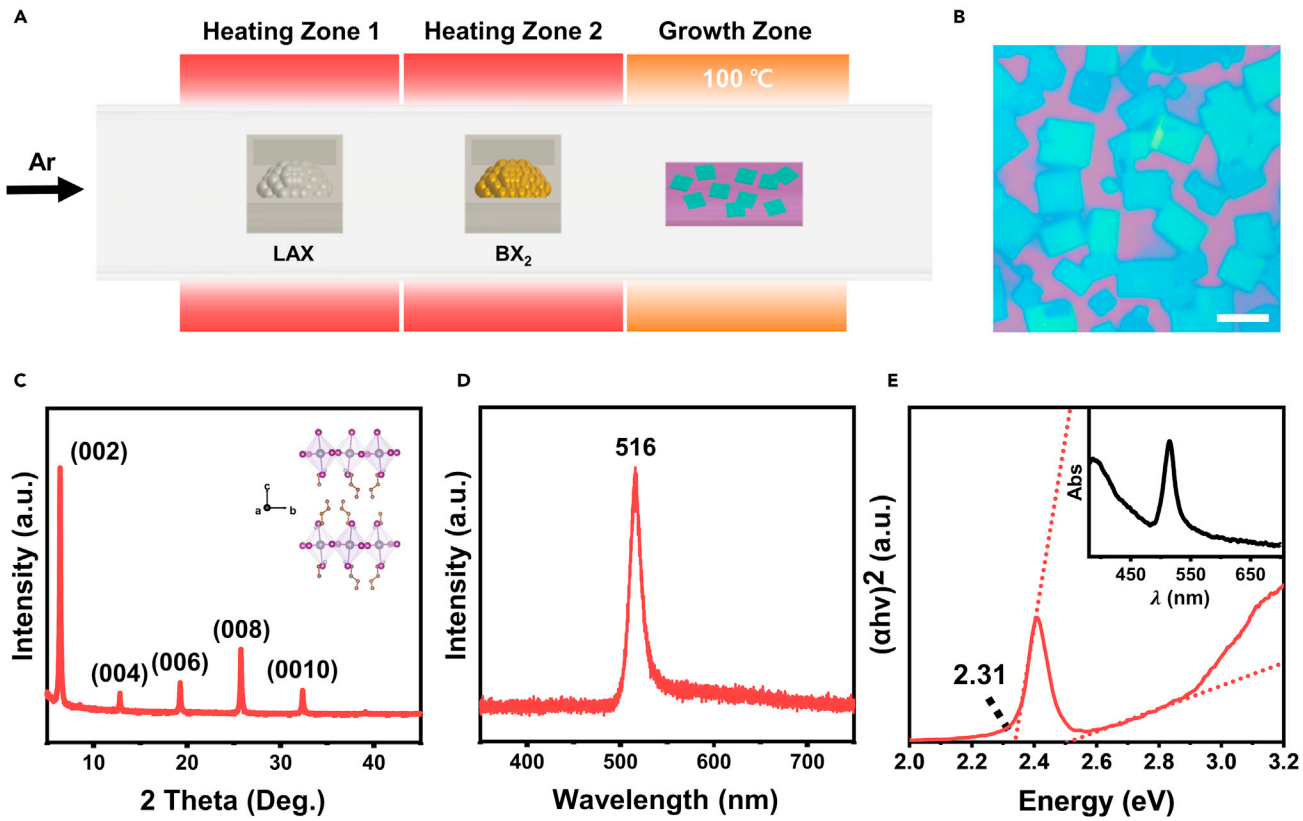

Figure 2. Schematics of three-heating-zone vapor deposition system and results of BA_2PbI_4 growth

(A) Schematic representation of the three-heating-zone CVD experimental setup to fabricate 2D (n = 1) perovskite nanoflakes.

(B) Optical microscope image of BA_2PbI_4 flakes grown on SiO_2/Si. Scale bar: 10 μm.

(C) XRD patterns of BA_2PbI_4 with illustration of the crystal structure.

(D) PL spectra of BA_2PbI_4.

(E) Absorption spectra of BA_2PbI_4 grown on c-plane sapphire. Inset shows absorbance data before converted into Tauc plot.

nanoflake growth. A three-heating-zone system was used to place an organic precursor, an inorganic precursor, and substrates separately in distinct zones, which were named heating zone 1, heating zone 2, and growth zone, respectively. Before RP perovskite growth, a quartz tube was thermally annealed at 300°C for 3 h. Two hundred milligrams of an organic precursor $C_4H_{12}IN$ (n-butylammonium iodide (BAI), Ossila, 98%) and 100 mg of a high-purity inorganic precursor (PbI_2, Sigma-Aldrich, 99.999% trace metal basis, perovskite grade) were filled in ceramic boats. Then, the BAI and PbI_2 boats were placed in heating zones 1 and 2, respectively. Placing the PbI_2 boat near the growth zone prevented PbI_2 from reacting with BAI during the supply and thereby, reduced the PbI_2 consumption. A substrate (Si wafer with 300-nm-thick SiO_2, mica, or c-plane sapphire layer) was placed in the center of the growth zone. During the growth, heating zones 1 and 2 were heated above 150°C, and the growth zone was maintained at a relatively low temperature of 100°C, which caused the following chemical reaction: $2BAI + PbI_2 \rightarrow BA_2PbI_4$. The reaction temperature of 100°C provided enough thermal energy for the large organic moiety (i.e., BAI) to diffuse well on the substrate. The as-formed BA_2PbI_4 molecules migrated to the edge or kink, which was the growth front of the flakes, without cluster formation. The entire process was performed in Ar atmosphere (see STAR Methods section for details). After 1 h of growth, randomly oriented rectangular nanoflakes were formed with high coverage and uniform color contrast (Figure 2B). The average thickness of randomly selected 80 samples is 46.0 nm with a standard deviation of 4.65 nm as presented in Figure S1, and the lateral size of the rectangular flakes ranged from 3.5 to 15.3 μm.

The X-ray diffraction (XRD) patterns clearly show that the grown material is BA_2PbI_4. The (002) peak appears at 6.49°, and the following (00l) peaks appear at intervals of 6.31° (Figure 2C). No peaks other than

the (00l) family are observed, indicating a perfectly c-axis-aligned structure. The *d*-spacing is determined to be 13.60 Å by $n\lambda = 2d\sin\theta$. This determined value refers to the distance between adjacent $[PbI_6]^{4-}$ inorganic slabs and agrees with the *d*-spacing value reported for the BA_2PbI_4 film fabricated by spin-coating (13.83 Å) (Cao et al., 2015). The slight deviation between the two values (−0.23 Å) is attributable to the slower crystallization process in CVD growth than in spin-coating, which allows enough time for the organic groups to be well aligned. This also results in sharp peaks, which indicate high crystallinity.

To investigate the optical properties of the BA_2PbI_4 flakes, photoluminescence (PL) measurement and ultraviolet-visible (UV-Vis) spectroscopy were performed at RT. The BA_2PbI_4 flakes exhibit an intense PL peak at 516 nm (corresponding to 2.40 eV) (Figure 2D), which is blue-shifted by 3 nm compared with the bulk (Dang et al., 2018). The peak shape is asymmetric, and a longer tail is observed on the low-energy side, which is in agreement with previous reports (Dou et al., 2015; Ni et al., 2017). Ni et al. reported that the asymmetric broadening on the low-energy side increases with the temperature, claiming that the asymmetric peak originates from self-trapped excitons formed by strong exciton–phonon coupling (Ni et al., 2017; Yuan et al., 2017). The full width at half maximum (FWHM) of the 516 nm peak was 16.6 nm (corresponding to 77 meV). The optical bandgap was calculated as 2.31 eV from the Tauc plot of the absorption spectrum (on c-plane sapphire) (Figure 2E). This value corresponds to the primary absorption edge, which indicates the first exciton transition. In 2D perovskites, the secondary absorption peak generally appears above the absorption edge region. This secondary absorption is caused by the long-lived exciton states trapped in the electric field generated between the positively charged BA^+ and negatively charged $[PbI_6]^{4-}$ (Cao et al., 2015).

Temperature-dependent growth

We systematically investigated the effects of growth temperature on the morphology of the grown perovskite films (Figure 3). The growth temperature was optimized based on the results of thermogravimetric analysis-differential scanning calorimetry (TGA-DSC). The TGA-DSC curves of organic and inorganic precursors (BAI and PbI_2, respectively) (Figures 3A–3C) exhibit weight loss and heat flow, respectively, with temperature. Both precursors were measured in an inert Ar atmosphere (Figures 3A and 3B). To study the effect of PbI_2 oxidation, we draw an additional TGA-DSC curve for PbI_2 under ambient conditions (Figure 3C). In the case of BAI, a heat absorption of 35.972 J/g occurs around the melting point of 173°C, and 100% weight loss is observed at 328.4°C (Figure S2A). The heat absorption of BAI occurs in multiple steps, indicating that the mass loss originates from a series of decomposition processes rather than one-step sublimation, with a large heat absorption of 609.47 J/g. Note that the heating temperature of BAI should be set as < 260°C, where heat absorption caused by decomposition begins gradually (Figure 3A). In the case of PbI_2, a heat absorption of 66.909 J/g occurs around the melting point of 402°C in both Ar and air. However, the decomposition in air starts at approximately 150°C lower than that in Ar (Figures S2B and S2C). Moreover, the decomposition in air comprises multiple exothermic and endothermic processes with the remaining residues, which can be some decomposition products or impurities. Considering the TGA-DSC results, the temperatures of heating zones 1 and 2 were set to 140–180°C and 280–320°C, respectively. Under these temperatures, the BAI powder could be steadily vaporized from heating zone 1; the vaporized BAI passed through heating zone 2 and reached the growth zone without decomposition. BAI vapor was not decomposed in heating zone 2 (280–320°C) as it quickly passed through heating zone 2. The temperature of heating zone 2 could sufficiently supply PbI_2 vapor for growth, but it was not too high to cause decomposition by air (decomposition onset temperature ~390°C in air).

The effects of heating temperature on the BA_2PbI_4 film morphology are shown in Figures 3D–3I. Under the different temperature conditions, the optimal film morphology is obtained at heating temperatures of 160°C and 310°C (for BAI and PbI_2, respectively) (Figure 3E). Under the optimized condition, the BA_2PbI_4 crystals are completely rectangular with uniform optical contrast, and the crystal size is relatively large (average lateral size of 9.36 μm). As the BAI heating temperature is decreased below 160°C, the crystal becomes more irregular and much smaller, leading to low surface coverage (Figures 3D and 3G). This morphology change is ascribed to the insufficient supply of BAI. Note that some PbI_2 residue is observed due to the off-stoichiometry. In contrast, as the BAI heating temperature is increased above 160°C, BAI is excessively supplied. In this case, the surplus BAI that has not reacted with PbI_2 destroys the rectangular crystal morphology and results in an irregular liquid-like curved morphology (Figures 3F and 3I). If excess PbI_2 is supplied, the crystallizations of PbI_2 (dominant at higher temperatures) and BA_2PbI_4 (dominant at lower temperatures) compete; at the BA_2PbI_4 crystallization temperature (i.e., at the growth zone temperature of 100°C, which is defined by the growth condition of Figure 3E), amorphous characteristics are shown by excess PbI_2, yielding a random morphology (Figure 3H). When excess PbI_2 is supplied, it tends to grow into an arbitrary shape, regardless of the BAI supply (Figures 3G and 3I).

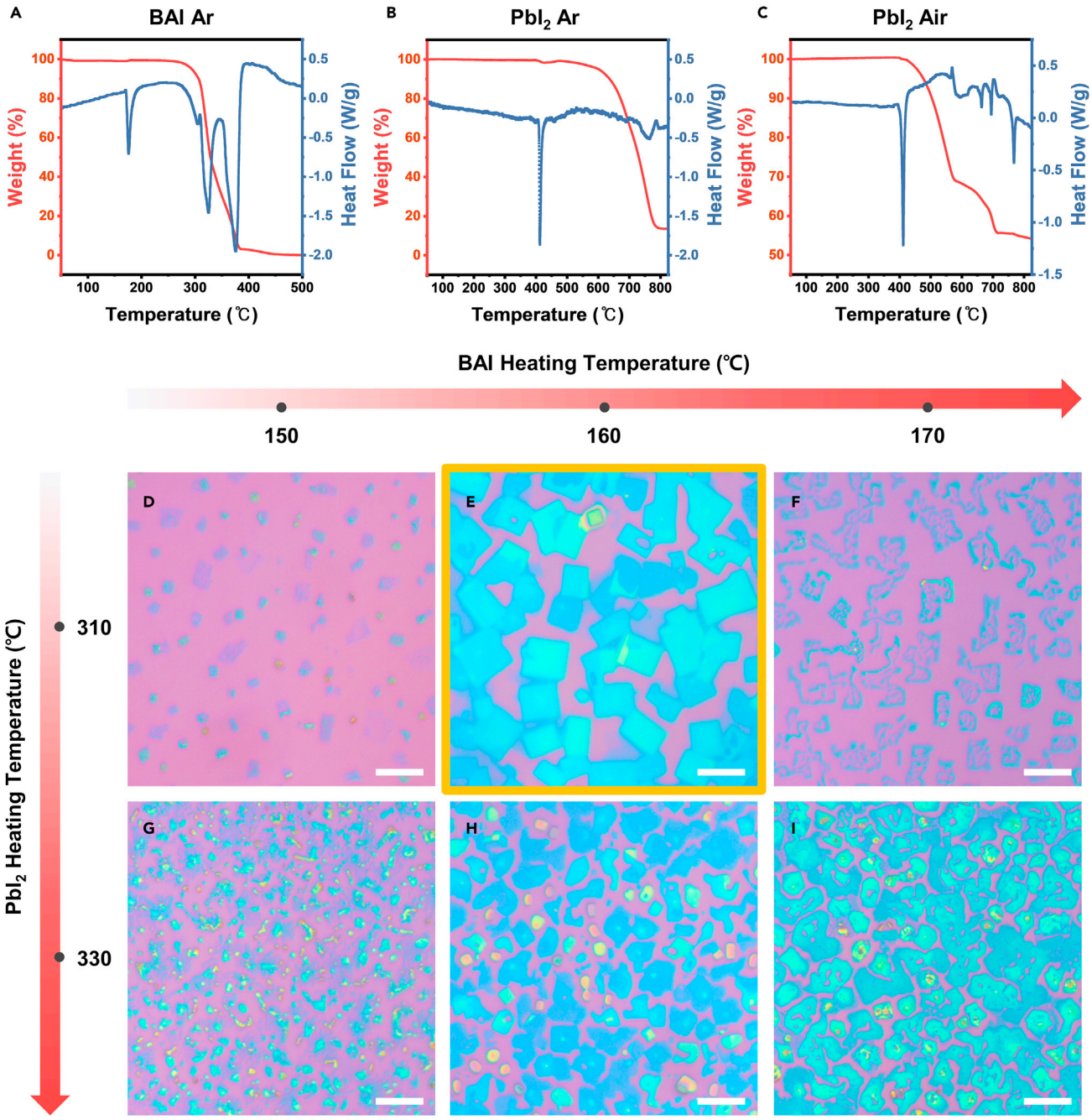

Figure 3. Temperature-dependent growth

(A) TGA-DSC data of n-butylammonium iodide under Ar atmosphere.

(B) TGA-DSC data of PbI_2 under Ar atmosphere.

(C) TGA-DSC data of PbI_2 under ambient condition.

(D–I) Heating-temperature-dependent morphologies of BA_2PbI_4 nanostructures. Scale bars: 10 μm.

Substrate-dependent growth

The substrate-dependent growth of 2D OIHP was studied by growing BA_2PbI_4 on different substrates: SiO_2/Si (Figure 3E), muscovite mica (Figure 4A), and c-plane sapphire (Figure 4B). Under optimal growth conditions (Table S1), the as-grown BA_2PbI_4 flakes show a well-defined rectangular shape for all substrates. Thickness distributions of 30 randomly selected BA_2PbI_4 flakes on mica and c-plane sapphire are

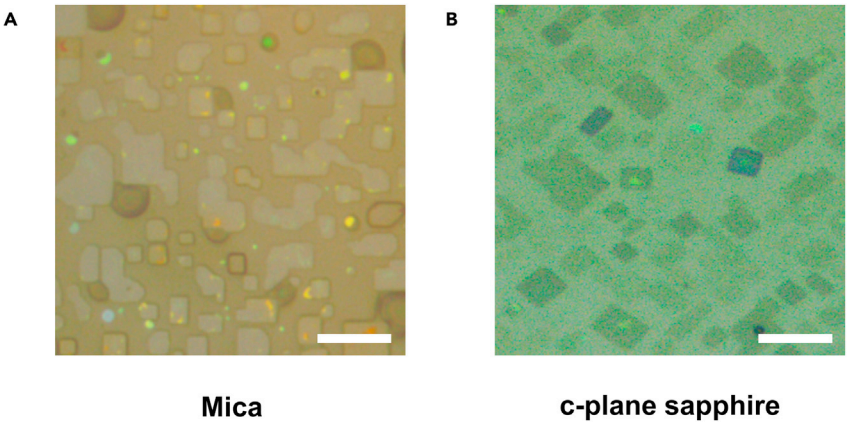

Figure 4. Substrate dependent growth

(A) Optical microscope image of BA_2PbI_4 flakes epitaxially grown on mica. Scale bar: 10 μm.

(B) Optical microscope image of BA_2PbI_4 flakes epitaxially grown on c-plane sapphire. Scale bar: 10 μm.

demonstrated in Figure S3. We deduce that the 2D OIHP can be epitaxially grown on various substrates without strict lattice matching conditions because LA cations bind on the substrate with a weak vdW interaction. In particular, the epitaxial growth of BA_2PbI_4 was demonstrated on the mica (Figure 4A) and c-plane sapphire (Figure 4B). In contrast to conventional epitaxy, which creates a strong bond between the film and substrate, the 2D OIHP is weakly coupled on mica and c-plane sapphire. Thus, the lattice matching condition of the 2D OIHP is less strict than other material systems. For mica, BA_2PbI_4 is coupled on the substrate through vdW epitaxy although the substrate and film have different symmetry; the space group of the mica is a monoclinic C2/c; however, the pseudo-hexagonal lattice on the (001) plane fits the 4-fold symmetry of BA_2PbI_4 by modifying the in-plane orientation of perovskite flakes. The schematic in Figure S4 exhibits the possible epitaxial relations of BA_2PbI_4[100]//mica[100] and BA_2PbI_4[010]//mica[010] with lattice mismatches of 14.64% and 3.98%, respectively. BA_2PbI_4[100] and mica[110] can also be aligned in the same way. A large lattice mismatch can be accommodated in the vdW epitaxy, which is a consistent result with the TMDC/TMDC and TMDC/graphene (Li et al., 2015). Similar to the mica, the orthorhombic BA_2PbI_4 was epitaxially grown on a trigonal c-plane sapphire by adjusting the in-plane orientation of flakes where the lattice mismatches are predicted to be 7.52% for BA_2PbI_4[100]//sapphire[100] and 4.70% for BA_2PbI_4[010]//sapphire[010].

Generality of the system: PbI_2 and PEA_2SnI_4 growth

We demonstrated that our CVD growth strategies are universal and applicable to other 2D perovskites as well, by studying PbI_2 and PEA_2SnI_4 growth mechanisms. The growth of PbI_2 with high crystallinity is essential for two reasons. First, PbI_2 is a layered material precursor capable of conversion into perovskite. The vapor phase synthesis of halide perovskites is largely divided into two methods—direct one-step growth and two-step growth—where BX_2 is deposited before the exposure of AX or LAX vapors. The latter is used to stack heterostructures by depositing BX_2 on a hydrophilic surface or a region with selectivity, such as TMDC, and to fabricate a perovskite patterned array by prepatterning BX_2. During the transformation, cations such as MAI and FAI are intercalated between the PbI_2 layers, and a reaction converting PbI_2 into perovskite occurs. Many protocols for converting PbI_2 into perovskites have been reported consistently (Ha et al., 2014; Liu et al., 2016; Niu et al., 2015). Second, PbI_2 itself functions as a 2D semiconducting material, which can be used in electronics and optoelectronics. PbI_2, belonging to the transition metal halide family, is an intrinsic p-type semiconductor and has a direct bandgap ranging from 2.3 to 2.6 eV in multilayer samples (Street et al., 1999). Ultrathin PbI_2 presents bandgap values in a range that cannot be covered by TMDC (Frisenda et al., 2017), making it a useful material for solar cells, photodetectors, and X-ray detectors (Shah et al., 1996; Xiao et al., 2019; Zhong et al., 2016). Moreover, each layer of PbI_2 comprises a dangling bond-free lattice and is weakly bound to the neighboring layers by vdW forces. This opens up the possibility of heterogeneous stacking with 2D layered materials, and the heterostructure may offer new physics phenomena and unique photophysical properties for novel optoelectronic applications.

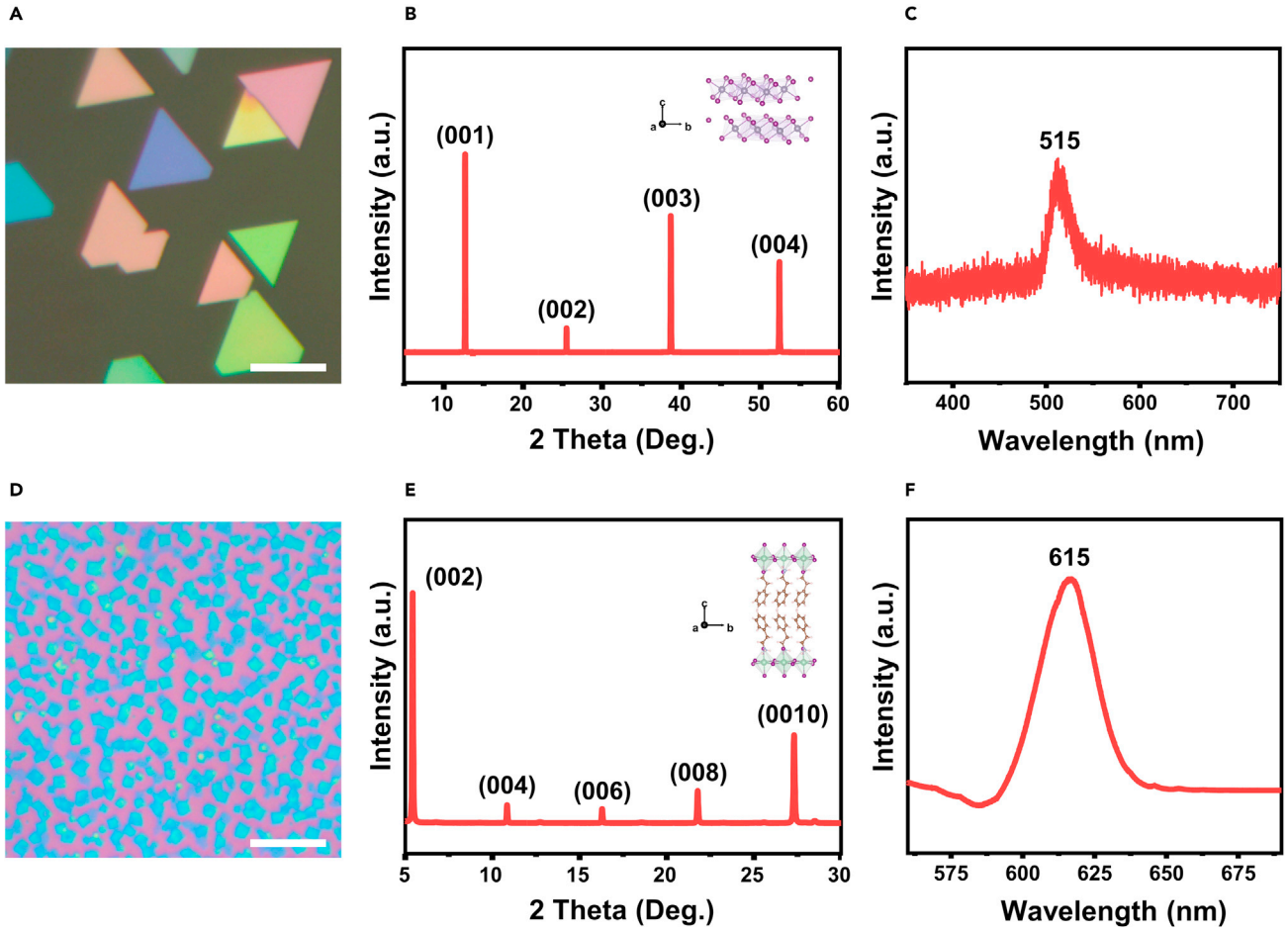

Figure 5. Generality of the system: PbI_2 and PEA_2SnI_4 growth

(A) Optical microscope image of PbI_2 flakes grown on mica. Scale bar: 10 μm.

(B) XRD patterns of PbI_2 with illustration of the crystal structure.

(C) PL spectra of PbI_2.

(D) Optical microscope image of PEA_2SnI_4 flakes grown on SiO_2/Si. Scale bar: 10 μm.

(E) XRD patterns of PEA_2SnI_4 with illustration of the crystal structure.

(F) PL spectra of PEA_2SnI_4.

PbI_2 was grown by a simple physical vapor deposition, where PbI_2 powder was vaporized from heating zone 2 (relatively high temperature) and deposited in heating zone 3 (relatively low temperature) (see STAR Methods section for details). The growth at 300°C for 20 min on mica yields epitaxially grown triangular domains (Figure 5A). The as-grown flakes have sharp edges, which indicates a high degree of crystallinity. The optical contrast between the flakes reveals thickness variation and the thickness of PbI_2 with different optical reflectance is measured by atomic force microscopy (AFM) (Figure S5). Both PbI_2 and mica have hexagonal lattice types on the (001) plane and show a well-matched lattice, which facilitates epitaxial growth of PbI_2 on mica (Wang et al., 2016). Lowering the temperature of heating zone 1 and increasing the growth time to 90 min can make PbI_2 grow into a full-coverage film (Figure S6).

To further investigate the structure and crystallinity of PbI_2, XRD patterns were measured and analyzed. The XRD pattern in Figure 5B confirms that the crystal is high-crystallinity 2H PbI_2, which is entirely c-axis oriented. The (001) peak at 12.71° indicates that the interlayer distance of PbI_2 is 6.965 Å, which agrees with the previously obtained results (Flahaut et al., 2006; JCPDS card no. 79-0803). It is also consistent with the fact that the 2H phase is stable at low temperature (<94°C), whereas the 12R phase is stable at high temperature (>94°C) (Palosz et al., 1987; Pałosz and Salje, 1989). The as-grown PbI_2 flakes exhibit a sharp PL spectrum with an emission peak at 515 nm (Figure 5C).

We further expanded our study toward a representative 2D lead-free perovskite, PEA_2SnI_4, to show that our CVD growth strategies can be employed for the synthesis of LA_2BX_4 perovskites with arbitrary LA and B cations. To the best of our knowledge, this is the first demonstration of CVD-grown PEA_2SnI_4. The organic precursor PEAI (GreatCell Solar, 99%) 100 mg and an inorganic precursor tin(II) iodide (SnI_2, Alfa Aesar, 99.999% metal basis, ultra-dry) 50 mg were placed in heating zones 1 and 2, respectively, similar to the BA_2PbI_4 growth. SiO_2/Si was positioned in the center of the growth zone. During the growth, heating zones 1 and 2 were heated beyond 150°C, and the growth zone was maintained at 110°C. Because the molecular weight of PEAI is larger than that of BAI, the temperature of the growth zone was set higher to make heavier PEAI diffuse well. In particular, the heating zone temperature was selected based on the TGA-DSC results (Figure S7). Heating zone 2 requires a temperature lower than its melting point (320°C) because SnI_2 undergoes $2SnI_2 + O_2 = SnO_2 + SnI_4(g)$ and $SnI_2 + O_2 = SnO_2 + I_2(g)$ reactions above the melting point. In addition, the temperature of the growth zone should be controlled to yield a chemical reaction of $2PEAI + SnI_2 \rightarrow PEA_2SnI_4$ and to prevent cluster formation on the substrate. All processes were conducted in an Ar atmosphere (see STAR Methods section for details). The optical microscope image in Figure 5D shows that rectangular crystals with a lateral size of up to 2 μm are formed after 1 h of growth. The crystal flakes are randomly oriented on SiO_2/Si with high coverage and uniform color contrast. To grow thinner flakes of larger size, a longer growth time and lower temperatures of heating zones 1 and 2 are required (Figure S8). The lower heating temperature can lead to slower vaporization of the precursors, offering sufficient time for the adatoms to diffuse to the edge of the flakes.

The XRD pattern reveals the crystal structure of PEA_2SnI_4 (Figure 5E). To obtain intense diffraction peaks, the thickness of the PEA_2SnI_4 film was intentionally increased. As a result, sharp (002) family peaks were obtained. The *d*-spacing calculated using the 2 θ value was 16.29 Å. Compared with BA_2PbI_4, the *d*-spacing was approximately 2.7 Å larger, mainly because of the difference in the length of LA cations. The PL emission of 615 nm suggests that the optical bandgap of PEA_2SnI_4 was 2.02 eV, which can be used as a red emitter. The FWHM was 21.9 nm (corresponding to ~70 meV), which was approximately 5 nm larger than that of the PL spectrum of BA_2PbI_4. This is attributable to the fact that Sn^{2+} is more rapidly oxidized to Sn^{4+} compared with Pb^{2+}, resulting in more Sn^{2+} vacancies and poor crystallinity of PEA_2SnI_4.

Conclusion

In summary, we report a general three-heating-zone one-step CVD growth strategy to synthesize high-crystallinity 2D (*n* = 1) RP perovskite single-crystal flakes and films. We demonstrated our method is universal by studying CVD growth of PbI_2, BA_2PbI_4, and PEA_2SnI_4. Especially, to the best of our knowledge, CVD growth of 2D lead-free perovskite PEA_2SnI_4 was demonstrated for the first time. BA_2PbI_4 was selected as a model system for growth mechanism study; the temperature of each heating zone was precisely controlled based on the result of TGA thermal analysis, not to decompose precursors on the way to the growth zone. The temperature of growth zone was set to a value that could make a reaction between organic and inorganic precursors to form perovskite, and resulting products sufficiently diffused without cluster formation. As a result, rectangular BA_2PbI_4 flakes were well formed on SiO_2/Si and c-plane sapphire, and the flakes were grown epitaxially on mica. Also, high-crystallinity PbI_2 flakes were deposited epitaxially on mica. Finally, the growth of lead-free tin-perovskite PEA_2SnI_4 had been achieved by substituting both organic and inorganic precursors. Our three-heating-zone system provides a universal route to grow 2D perovskites based on various LA organic cations and B divalent metal cations and has a great potential for future electronics and optoelectronics applications.

Limitations of the study

We report a three-heating-zone CVD system for high-crystallinity 2D (n = 1) perovskite single crystal flakes and films growth, and CVD growth of 2D lead-free perovskite PEA_2SnI_4 was demonstrated. 2D (n = 1) perovskite possesses improved chemical and thermal stability compared with 3D perovskite; however, semiconductor industry still requires better stability. We envision that 2D perovskite will be utilized actively in flexible electronics, internet of things system, and so forth by taking advantage of its low temperature crystallization.

STAR★METHODS

Detailed methods are provided in the online version of this paper and include the following:

- KEY RESOURCES TABLE

SUPPLEMENTAL INFORMATION

Supplemental information can be found online at https://doi.org/10.1016/j.isci.2021.103486.

ACKNOWLEDGMENTS

This work was supported by the National Research Foundation of Korea (NRF) grant funded by the Korea government (MSIT) (2020M3F3A2A01082618, 2021R1C1C1007292, 2021R1F1A1062140), Korea Institute of Science and Technology (KIST) Institutional Program (2V07080-19-P148), and POSCO Science fellowship.

AUTHOR CONTRIBUTIONS

A.H. performed the synthesis and characterization of the materials. A.H., T.S.K., and M.K. set up the chemical vapor deposition system. The manuscript was written by A.H., H.C., and K.K. All authors discussed the results and commented on the manuscript.

DECLARATION OF INTERESTS

The authors declare no competing interests.

Received: July 6, 2021
Revised: October 6, 2021
Accepted: November 19, 2021
Published: December 17, 2021

REFERENCES

Ball, J.M., and Petrozza, A. (2016). Defects in perovskite-halides and their effects in solar cells. Nat. Energy *1*. https://doi.org/10.1038/nenergy.2016.149.

Brehier, A., Parashkov, R., Lauret, J.S., and Deleporte, E. (2006). Strong exciton-photon coupling in a microcavity containing layered perovskite semiconductors. Appl. Phys. Lett. *89*. https://doi.org/10.1063/1.2369533.

Cao, D.H., Stoumpos, C.C., Farha, O.K., Hupp, J.T., and Kanatzidis, M.G. (2015). 2D Homologous perovskites as light-absorbing materials for solar cell applications. J. Am. Chem. Soc. *137*, 7843–7850. https://doi.org/10.1021/jacs.5b03796.

Cao, D.H., Stoumpos, C.C., Yokoyama, T., Logsdon, J.L., Song, T. Bin, Farha, O.K., Wasielewski, M.R., Hupp, J.T., and Kanatzidis, M.G. (2017). Thin films and solar cells based on semiconducting two-dimensional Ruddlesden-Popper $(CH_3(CH_2)_3NH_3)_2(CH_3NH_3)_{n-1}Sn_nI_{3n+1}$ perovskites. ACS Energy Lett. *2*, 982–990. https://doi.org/10.1021/acsenergylett.7b00202.

Chen, Y., Sun, Y., Peng, J., Zhang, W., Su, X., Zheng, K., Pullerits, T., and Liang, Z. (2017a). Tailoring organic cation of 2D air-stable organometal halide perovskites for highly efficient planar solar cells. Adv. Energy Mater. *7*, 1–7. https://doi.org/10.1002/aenm.201700162.

Chen, Z., Wang, Y., Sun, X., Guo, Y., Hu, Y., Wertz, E., Wang, X., Gao, H., Lu, T.M., and Shi, J. (2017b). Van der Waals hybrid perovskite of high optical quality by chemical vapor deposition. Adv. Opt. Mater. *5*, 1–8. https://doi.org/10.1002/adom.201700373.

Cheng, P., Wu, T., Zhang, J., Li, Y., Liu, J., Jiang, L., Mao, X., Lu, R.F., Deng, W.Q., and Han, K. (2017). $(C_6H_5C_2H_4NH_3)_2GeI_4$: a layered two-dimensional perovskite with potential for photovoltaic applications. J. Phys. Chem. Lett. *8*, 4402–4406. https://doi.org/10.1021/acs.jpclett.7b01985.

Cho, H., Jeong, S.H., Park, M.H., Kim, Y.H., Wolf, C., Lee, C.L., Heo, J.H., Sadhanala, A., Myoung, N.S., Yoo, S., et al. (2015). Overcoming the electroluminescence efficiency limitations of perovskite light-emitting diodes. Science *350*, 1222–1225. https://doi.org/10.1126/science.aad1818.

Cho, H., Kim, Y.H., Wolf, C., Lee, H.D., and Lee, T.W. (2018). Improving the stability of metal halide perovskite materials and light-emitting diodes. Adv. Mater. *30*, 1–24. https://doi.org/10.1002/adma.201704587.

Conings, B., Drijkoningen, J., Gauquelin, N., Babayigit, A., D'Haen, J., D'Olieslaeger, L., Ethirajan, A., Verbeeck, J., Manca, J., Mosconi, E., et al. (2015). Intrinsic thermal instability of methylammonium lead trihalide perovskite. Adv. Energy Mater. *5*, 1–8. https://doi.org/10.1002/aenm.201500477.

Dang, Y., Wei, J., Liu, X., Wang, X., Xu, K., Lei, M., Hu, W., and Tao, X. (2018). Layered hybrid perovskite solar cells based on single-crystalline precursor solutions with superior reproducibility. Sustain. Energy Fuels *2*, 2237–2243. https://doi.org/10.1039/c8se00213d.

Dou, L., Wong, A.B., Yu, Y., Lai, M., Kornienko, N., Eaton, S.W., Fu, A., Bischak, C.G., Ma, J., Ding, T., et al. (2015). Atomically thin two-dimensional Organic-inorganic hybrid perovskites. Science *349*, 1518–1521. https://doi.org/10.1126/science.aac7660.

Eames, C., Frost, J.M., Barnes, P.R.F., O'Regan, B.C., Walsh, A., and Islam, M.S. (2015). Ionic transport in hybrid lead iodide perovskite solar cells. Nat. Commun. *6*, 2–9. https://doi.org/10.1038/ncomms8497.

Fakharuddin, A., Qiu, W., Croes, G., Devižis, A., Gegevičius, R., Vakhnin, A., Rolin, C., Genoe, J., Gehlhaar, R., Kadashchuk, A., et al. (2019). Reduced efficiency roll-off and improved stability of mixed 2D/3D perovskite light emitting diodes by balancing charge injection. Adv. Funct. Mater. *29*, 1–12. https://doi.org/10.1002/adfm.201904101.

Flahaut, E., Sloan, J., Friedrichs, S., Kirkland, A.I., Coleman, K.S., Williams, V.C., Hanson, N., Hutchison, J.L., and Green, M.L.H. (2006). Crystallization of 2H and 4H PbI_2 in carbon nanotubes of varying diameters and morphologies. Chem. Mater. *18*, 2059–2069. https://doi.org/10.1021/cm0526056.

Frisenda, R., Island, J.O., Lado, J.L., Giovanelli, E., Gant, P., Nagler, P., Bange, S., Lupton, J.M., Schüller, C., Molina-Mendoza, A.J., et al. (2017). Characterization of highly crystalline lead iodide nanosheets prepared by room-temperature solution processing. Nanotechnology *28*. https://doi.org/10.1088/1361-6528/aa8e5c.

Gao, Y., Shi, E., Deng, S., Shiring, S.B., Snaider, J.M., Liang, C., Yuan, B., Song, R., Janke, S.M., Liebman-Peláez, A., et al. (2019a). Molecular engineering of organic–inorganic hybrid perovskites quantum wells. Nat. Chem. *11*, 1151–1157. https://doi.org/10.1038/s41557-019-0354-2.

Gao, Y., Wei, Z., Yoo, P., Shi, E., Zeller, M., Zhu, C., Liao, P., and Dou, L. (2019b). Highly stable lead-free perovskite field-effect transistors incorporating linear Π-conjugated organic ligands. J. Am. Chem. Soc. *141*, 15577–15585. https://doi.org/10.1021/jacs.9b06276.

Gélvez-Rueda, M.C., Hutter, E.M., Cao, D.H., Renaud, N., Stoumpos, C.C., Hupp, J.T., Savenije, T.J., Kanatzidis, M.G., and Grozema, F.C. (2017). Interconversion between free charges and bound excitons in 2D hybrid lead halide perovskites. J. Phys. Chem. C *121*, 26566–26574. https://doi.org/10.1021/acs.jpcc.7b10705.

Ghoshal, D., Wang, T., Tsai, H., Chang, S., and Crommie, M. (2019). Catalyst-Free and Morphology-Controlled Growth of 2D Perovskite Nanowires for Polarized Light Detection. Adv. Opt. Mater. 1–7. https://doi.org/10.1002/adom.201900039.

Grancini, G., Roldán-Carmona, C., Zimmermann, I., Mosconi, E., Lee, X., Martineau, D., Narbey, S., Oswald, F., De Angelis, F., Graetzel, M., and Nazeeruddin, M.K. (2017). One-Year stable perovskite solar cells by 2D/3D interface engineering. Nat. Commun. *8*, 1–8. https://doi.org/10.1038/ncomms15684.

Ha, S.T., Liu, X., Zhang, Q., Giovanni, D., Sum, T.C., and Xiong, Q. (2014). Synthesis of organic-inorganic lead halide perovskite nanoplatelets: towards high-performance perovskite solar cells and optoelectronic devices. Adv. Opt. Mater. *2*, 838–844. https://doi.org/10.1002/adom.201400106.

Hao, F., Stoumpos, C.C., Chang, R.P.H., and Kanatzidis, M.G. (2014). Anomalous band gap behavior in mixed Sn and Pb perovskites enables broadening of absorption spectrum in solar cells. J. Am. Chem. Soc. *136*, 8094–8099. https://doi.org/10.1021/ja5033259.

Hao, F., Stoumpos, C.C., Guo, P., Zhou, N., Marks, T.J., Chang, R.P.H., and Kanatzidis, M.G. (2015). Solvent-mediated crystallization of $CH_3NH_3SnI_3$ films for heterojunction depleted perovskite solar cells. J. Am. Chem. Soc. *137*, 11445–11452. https://doi.org/10.1021/jacs.5b06658.

Haque, M.A., Kee, S., Villalva, D.R., Ong, W.L., and Baran, D. (2020). Halide perovskites: thermal transport and prospects for thermoelectricity. Adv. Sci. *7*. https://doi.org/10.1002/advs.201903389.

Hill, H.M., Rigosi, A.F., Roquelet, C., Chernikov, A., Berkelbach, T.C., Reichman, D.R., Hybertsen, M.S., Brus, L.E., and Heinz, T.F. (2015). Observation of excitonic rydberg states in monolayer MoS_2 and WS_2 by photoluminescence excitation spectroscopy. Nano Lett. *15*, 2992–2997. https://doi.org/10.1021/nl504868p.

Huang, J., Tan, S., Lund, P.D., and Zhou, H. (2017). Impact of H_2O on organic-inorganic hybrid perovskite solar cells. Energy Environ. Sci. *10*, 2284–2311. https://doi.org/10.1039/c7ee01674c.

Jang, Y.W., Lee, S., Yeom, K.M., Jeong, K., Choi, K., Choi, M., and Noh, J.H. (2021). Intact 2D/3D halide junction perovskite solar cells via solid-phase in-plane growth. Nat. Energy *6*, 63–71. https://doi.org/10.1038/s41560-020-00749-7.

Kaltenbrunner, M., Adam, G., Głowacki, E.D., Drack, M., Schwödiauer, R., Leonat, L., Apaydin, D.H., Groiss, H., Scharber, M.C., White, M.S., et al. (2015). Flexible high power-per-weight perovskite solar cells with chromium oxide-metal contacts for improved stability in air. Nat. Mater. *14*, 1032–1039. https://doi.org/10.1038/nmat4388.

Lai, M., Obliger, A., Lu, D., Kley, C.S., Bischak, C.G., Kong, Q., Lei, T., Dou, L., Ginsberg, N.S., Limmer, D.T., and Yang, P. (2018). Intrinsic anion diffusivity in lead halide perovskites is facilitated by a soft lattice. Proc. Natl. Acad. Sci. United States America *115*, 11929–11934. https://doi.org/10.1073/pnas.1812718115.

Lee, H.D., Kim, H., Cho, H., Cha, W., Hong, Y., Kim, Y.H., Sadhanala, A., Venugopalan, V., Kim, J.S., Choi, J.W., et al. (2019). Efficient Ruddlesden–Popper perovskite light-emitting diodes with randomly oriented nanocrystals. Adv. Funct. Mater. *29*. https://doi.org/10.1002/adfm.201901225.

Li, M.Y., Shi, Y., Cheng, C.C., Lu, L.S., Lin, Y.C., Tang, H.L., Tsai, M.L., Chu, C.W., Wei, K.H., He, J.H., et al. (2015). Epitaxial growth of a monolayer WSe_2-MoS_2 lateral p-n junction with an atomically sharp interface. Science *349*, 524–528. https://doi.org/10.1126/science.aab4097.

Lin, Y., Bai, Y., Fang, Y., Chen, Z., Yang, S., Zheng, X., Tang, S., Liu, Y., Zhao, J., and Huang, J. (2018). Enhanced thermal stability in perovskite solar cells by assembling 2D/3D stacking structures. J. Phys. Chem. Lett. *9*, 654–658. https://doi.org/10.1021/acs.jpclett.7b02679.

Liu, J., Xue, Y., Wang, Z., Xu, Z.Q., Zheng, C., Weber, B., Song, J., Wang, Y., Lu, Y., Zhang, Y., and Bao, Q. (2016). Two-dimensional $CH_3NH_3PbI_3$ perovskite: synthesis and optoelectronic application. ACS Nano *10*, 3536–3542. https://doi.org/10.1021/acsnano.5b07791.

Liu, M., Johnston, M.B., and Snaith, H.J. (2013). Efficient planar heterojunction perovskite solar cells by vapour deposition. Nature *501*, 395–398. https://doi.org/10.1038/nature12509.

Luo, P., Zhou, S., Xia, W., Cheng, J., Xu, C., and Lu, Y. (2017). Chemical vapor deposition of perovskites for photovoltaic application. Adv. Mater. Inter. *4*. https://doi.org/10.1002/admi.201600970.

Matsushima, T., Hwang, S., Sandanayaka, A.S.D., Qin, C., Terakawa, S., Fujihara, T., Yahiro, M., and Adachi, C. (2016). Solution-Processed organic–inorganic perovskite field-effect transistors with high hole mobilities. Adv. Mater. *28*, 10275–10281. https://doi.org/10.1002/adma.201603126.

McMeekin, D.P., Sadoughi, G., Rehman, W., Eperon, G.E., Saliba, M., Hörantner, M.T., Haghighirad, A., Sakai, N., Korte, L., Rech, B., et al. (2016). A mixed-cation lead mixed-halide perovskite absorber for tandem solar cells. Science *351*, 151–155. https://doi.org/10.1126/science.aad5845.

Ni, L., Huynh, U., Cheminal, A., Thomas, T.H., Shivanna, R., Hinrichsen, T.F., Ahmad, S., Sadhanala, A., and Rao, A. (2017). Real-time observation of exciton-phonon coupling dynamics in self-assembled hybrid perovskite quantum wells. ACS Nano *11*, 10834–10843. https://doi.org/10.1021/acsnano.7b03984.

Ning, W., and Gao, F. (2019). Structural and functional diversity in lead-free halide perovskite materials. Adv. Mater. *31*, 1–21. https://doi.org/10.1002/adma.201900326.

Niu, L., Liu, X., Cong, C., Wu, C., Wu, D., Chang, T.R., Wang, H., Zeng, Q., Zhou, J., Wang, X., et al. (2015). Controlled synthesis of organic/inorganic van der Waals solid for tunable light-matter interactions. Adv. Mater. *27*, 7800–7808. https://doi.org/10.1002/adma.201503367.

Pałosz, B., and Salje, E. (1989). Lattice parameters and spontaneous strain in AX_2 polytypes: CdI_2 , PbI_2, SnS_2 and $SnSe_2$. J. Appl. Crystallogr. *22*, 622–623. https://doi.org/10.1107/s0021889889006916.

Palosz, B., Winkler, B., Dove, M.T., Cheng, C., Needs, R.J., and Heine, V. (1987). In situ observation of the polytypic phase transition 2H-12R in PbI_2 : investigations of the thermodynamic structural and dielectric properties. J. Phys. C : Solid State Phys. *20*, 4077–4096. https://doi.org/10.1088/0022-3719/20/26/011.

Pan, D., Fu, Y., Spitha, N., Zhao, Y., Roy, C.R., Morrow, D.J., Kohler, D.D., Wright, J.C., and Jin, S. (2021). Deterministic fabrication of arbitrary vertical heterostructures of two-dimensional Ruddlesden–Popper halide perovskites. Nat. Nanotechnol. *16*, 159–165. https://doi.org/10.1038/s41565-020-00802-2.

Shah, K.S., Olschner, F., Moy, L.P., Bennett, P., Misra, M., Zhang, J., Squillante, M.R., and Lund, J.C. (1996). Lead iodide X-ray detection systems. Nucl. Instr. Methods Phys. Res. Section A: Acc. Spectromet. Detect. Ass. Equip. *380*, 266–270. https://doi.org/10.1016/S0168-9002(96)00346-4.

Smith, I.C., Hoke, E.T., Solis-Ibarra, D., McGehee, M.D., and Karunadasa, H.I. (2014). A layered hybrid perovskite solar-cell absorber with enhanced moisture stability. Angew. Chem. *126*, 11414–11417. https://doi.org/10.1002/ange.201406466.

Song, C., Noh, G., Kim, T.S., Kang, M., Song, H., Ham, A., Jo, M.K., Cho, S., Chai, H.J., Cho, S.R., et al. (2020). Growth and interlayer engineering of 2D layered semiconductors for future electronics. ACS Nano *14*, 16266–16300. https://doi.org/10.1021/acsnano.0c06607.

Street, R.A., Ready, S.E., Lemmi, F., Shah, K.S., Bennett, P., and Dmitriyev, Y. (1999). Electronic transport in polycrystalline PbI_2 films. J. Appl. Phys. *86*, 2660–2667. https://doi.org/10.1063/1.371107.

Tan, Z., Wu, Y., Hong, H., Yin, J., Zhang, J., Lin, L., Wang, M., Sun, X., Sun, L., Huang, Y., et al. (2016). Two-dimensional $(C_4H_9NH_3)_2PbBr_4$ perovskite crystals for high-performance photodetector. J. Am. Chem. Soc. *138*, 16612–16615. https://doi.org/10.1021/jacs.6b11683.

Tsai, H., Asadpour, R., Blancon, J.C., Stoumpos, C.C., Even, J., Ajayan, P.M., Kanatzidis, M.G., Alam, M.A., Mohite, A.D., and Nie, W. (2018). Design principles for electronic charge transport in solution-processed vertically stacked 2D perovskite quantum wells. Nat. Commun. *9*, 1–9. https://doi.org/10.1038/s41467-018-04430-2.

Wang, Y., Sun, Y.Y., Zhang, S., Lu, T.M., and Shi, J. (2016). Band gap engineering of a soft inorganic compound PbI_2 by incommensurate van der Waals epitaxy. Appl. Phys. Lett. *108*. https://doi.org/10.1063/1.4939269.

Wang, Z., Lin, Q., Chmiel, F.P., Sakai, N., Herz, L.M., and Snaith, H.J. (2017). Efficient ambient-air-stable solar cells with 2D-3D heterostructured butylammonium-caesium-formamidinium lead halide perovskites. Nat. Energy *2*, 1–10. https://doi.org/10.1038/nenergy.2017.135.

Xiao, H., Liang, T., and Xu, M. (2019). Growth of ultraflat PbI_2 nanoflakes by solvent evaporation suppression for high-performance UV photodetectors. Small *15*, 1–7. https://doi.org/10.1002/smll.201901767.

Yang, X., Héroux, J.B., Mei, L.F., and Wang, W.I. (2001). InGaAsNSb/GaAs quantum wells for 1.55 μm lasers grown by molecular-beam epitaxy. Appl. Phys. Lett. *78*, 4068–4070. https://doi.org/10.1063/1.1379787.

Yang, X., Zhang, X., Deng, J., Chu, Z., Jiang, Q., Meng, J., Wang, P., Zhang, L., Yin, Z., and You, J. (2018). Efficient green light-emitting diodes based on quasi-two-dimensional composition and phase engineered perovskite with surface passivation. Nat. Commun. *9*, 2–9. https://doi.org/10.1038/s41467-018-02978-7.

Ye, H.Y., Liao, W.Q., Hu, C.L., Zhang, Y., You, Y.M., Mao, J.G., Li, P.F., and Xiong, R.G. (2016). Bandgap engineering of lead-halide perovskite-type ferroelectrics. Adv. Mater. *28*, 2579–2586. https://doi.org/10.1002/adma.201505224.

Yokoyama, T., Cao, D.H., Stoumpos, C.C., Song, T.B., Sato, Y., Aramaki, S., and Kanatzidis, M.G. (2016). Overcoming short-circuit in lead-free $CH_3NH_3SnI_3$ perovskite solar cells via kinetically controlled gas-solid reaction film fabrication process. J. Phys. Chem. Lett. *7*, 776–782. https://doi.org/10.1021/acs.jpclett.6b00118.

Yuan, M., Quan, L.N., Comin, R., Walters, G., Sabatini, R., Voznyy, O., Hoogland, S., Zhao, Y., Beauregard, E.M., Kanjanaboos, P., et al. (2016). Perovskite energy funnels for efficient light-emitting diodes. Nat. Nanotechnol. *11*, 872–877. https://doi.org/10.1038/nnano.2016.110.

Yuan, Z., Zhou, C., Tian, Y., Shu, Y., Messier, J., Wang, J.C., Van De Burgt, L.J., Kountouriotis, K., Xin, Y., Holt, E., et al. (2017). One-dimensional organic lead halide perovskites with efficient bluish white-light emission. Nat. Commun. *8*. https://doi.org/10.1038/ncomms14051.

Zhang, Q., Chu, L., Zhou, F., Ji, W., and Eda, G. (2018). Excitonic properties of chemically synthesized 2D organic–inorganic hybrid perovskite nanosheets. Adv. Mater. *30*, 1–8. https://doi.org/10.1002/adma.201704055.

Zhong, M., Huang, L., Deng, H.X., Wang, X., Li, B., Wei, Z., and Li, J. (2016). Flexible photodetectors based on phase dependent PbI_2 single crystals. J. Mater. Chem. C *4*, 6492–6499. https://doi.org/10.1039/c6tc00918b.

STAR★METHODS

KEY RESOURCES TABLE

REAGENT or RESOURCE	SOURCE	IDENTIFIER
Chemicals, peptides, and recombinant proteins		
n-Butylammonium Iodide	Ossila	CAS: 36945-08-1
Lead(II) Iodide	Sigma-Aldrich	CAS: 10101-63-0
Phenethylammonium Iodide	Greatcell Solar	CAS: 151059-43-7
Tin(II) Iodide	Alfa Aesar	CAS: 10294-70-9
Software and algorithms		
XEI	Park Systems	http://parksystems.com
VESTA 3.5.7	JP-Minerals	http://jp-minerals.org/vesta
Origin 2019	Originlab	http://www.originlab.com

RESOURCE AVAILABILITY

Lead contact

Further information and requests for resources and reagents should be directed to and will be fulfilled by the lead contact, Kibum Kang (kibumkang@kaist.ac.kr).

Materials availability

This study did not generate new unique reagents.

Data and code availability

All data reported in this paper will be shared by the lead contact upon request.

This paper does not report original code.

All software's used in this study are commercially available.

Any additional information required to reanalyze the data reported in this work paper is available from the Lead Contact upon request.

EXPERIMENTAL MODEL AND SUBJECT DETAILS

Vapor deposition of BA_2PbI_4

BA_2PbI_4 was grown using a three-heating-zone system to separately place organic precursor, inorganic precursor and substrates in distinct zones with 1 in. diameter quartz tube. The organic precursor $C_4H_{12}IN$ (BAI) 200 mg and inorganic precursor PbI_2 100 mg were loaded in ceramic boats and were placed in the heating zone 1 and the heating zone 2, respectively. A substrate (Si wafer with 300 nm-thick SiO_2, freshly cleaved muscovite mica or c-plane sapphire) was placed in the center of the growth zone. During the growth on SiO_2/Si, the heating zone 1 and the heating zone 2 were heated to 160°C and 300°C, respectively, and the growth zone was kept at a temperature of 100°C. During the growth on mica and c-plane sapphire, the heating zone 1 and the heating zone 2 were heated to 160°C and 350°C, respectively, and the growth zone was kept at a temperature of 100°C. After reaching the given temperature, 99.999% Ar was flowed in at 200 sccm and pressure was stabilized at 8.9×10^{-1} Torr in all three cases. Growth was carried out for 1 h, and furnace was cooled down without Ar flowing.

Vapor deposition of PbI_2

PbI_2 was grown using a heating zone 2 and growth zone of three-heating-zone system with 1 in. diameter quartz tube. The inorganic precursor PbI_2 100 mg and mica were placed in the heating zone 2 and the growth zone, respectively. Heating zone 2 was heated to 370°C and the growth zone was heated to

300°C within 20 min and kept for 1 min. During the growth, 99.999% Ar was flowed in at 15 sccm and pressure was stabilized at 1.3×10^{0} Torr.

Vapor deposition of PEA_2SnI_4

For PEA_2SnI_4 growth, the organic precursor $C_8H_{12}IN$ (PEAI) 100 mg and inorganic precursor SnI_2 50 mg were loaded in ceramic boats and were placed in the heating zone 1 and the heating zone 2, respectively. A Si wafer with 300 nm-thick SiO_2 was placed in the center of the growth zone. The heating zone 1 and the heating zone 2 were heated to 165°C and 275°C, respectively, and the growth zone was kept at a temperature of 110°C. During the growth, 99.999% Ar was flowed in at 50 sccm and pressure was stabilized at 2.7×10^{-1} Torr. Growth was carried out for 1 h, and furnace was cooled down without Ar flowing.

METHOD DETAILS

Materials

The powders used to grow BA_2PbI_4, PbI_2, and PEA_2SnI_4 were $C_4H_{12}IN$ (n-Butylammonium Iodide, BAI, Ossila, 98%), PbI_2 (Lead(II) Iodide, Sigma-Aldrich, 99.999% trace metals basis, perovskite grade), $C_8H_{12}IN$ (Phenethylammonium Iodide, PEAI, Greatcell Solar, 99%), and SnI_2 (Tin(II) Iodide, Alfa Aesar, 99.999% metals basis, ultra-dry).

Growth

The growth strategies for the BA_2PbI_4, PbI_2, and PEA_2SnI_4 are explained in detail under the section "experimental model and subject details" with respective subheading.

Material characterization

Detailed methods of characterizations are introduced in the "quantification and statistical analysis" section.

Statistical analysis

The statistical analysis of the thickness distribution was conducted with AFM measurements and details are given in the section "quantification and statistical analysis".

QUANTIFICATION AND STATISTICAL ANALYSIS

Material characterization

Optical microscope images were captured with Olympus BX 53M microscope. XRD 2θ scans were conducted using a Rigaku SmartLab instrument with a Cu-Kα radiation source (1.5406 Å) operating at a voltage of 45 kV and a current of 200 mA. UV-Vis absorption measurements were carried out using a SolidSpec-3700i/3700iDUV with a PMT, InGaAs and PbS detectors attached to the integrating sphere. PL spectra were measured with HORIBA LabRAM HR Evolution Visible-NIR (325 nm wavelength laser) for BA_2PbI_4 and PbI_2 measurements and Horiba ARAMIS (514 nm wavelength laser) for PEA_2SnI_4 measurement. The Si peak at 521 cm^{-1} was used for calibration in the data analysis of the spectra. TGA-DSC experiments were analyzed using LABSIS Evo and TGA-DTG experiments were analyzed using TG209 F1 Libra. 10 mg of sample was used for each run with a heating rate of 20°C min^{-1}. SEM image was collected in secondary electron mode by a Hitachi S4800. AFM measurements were done using Park NX10.

Statistical analysis

The thickness distribution on SiO_2/Si was measured for 80 flakes on the identical substrate grown under the optimized conditions. 80 samples were randomly selected from those grown in the center of the substrate. The flake thickness was measured using XEI. Due to the thickness variation within one flake, the thickness was extracted as a difference in height between the substrate and the highest point. For mica and c-plane sapphire, the thickness distribution was measured for 30 flakes on the identical substrate grown under the optimized conditions. The thickness extraction rule was the same as in the case of SiO_2/Si.

Software

Molecular models were drawn using VESTA 3.5.7, and all the graphs were plotted using Origin 2019.